Quantum metal state and quantum phase transitions in type-II Ising superconducting films

Yi Liu,[1,2]* Yong Xu,[2,3]* Jian Sun,[1,2]* Chong Liu,[3]* Yanzhao Liu,[1,2] Chong Wang,[2,3,4] Zetao Zhang,[2,3] Kaiyuan Gu,[1,2] Yue Tang,[1,2] Cui Ding,[3] Haiwen Liu,[5] Hong Yao,[2,3,4] Xi Lin,[1,2,6,7]† Lili Wang,[2,3]† Qikun Xue,[2,3,6] Jian Wang[1,2,3,6,7]†

[1]International Center for Quantum Materials, School of Physics, Peking University, Beijing 100871, China.

[2]Collaborative Innovation Center of Quantum Matter, Beijing 100871, China.

[3]State Key Laboratory of Low-Dimensional Quantum Physics, Department of Physics, Tsinghua University, Beijing 100084, China.

[4]Institute for Advanced Study, Tsinghua University, Beijing 100084, China.

[5]Center for Advanced Quantum Studies, Department of Physics, Beijing Normal University, Beijing 100875, China.

[6]Beijing Academy of Quantum Information Sciences, West Bld. #3, No. 10 Xibeiwang East Rd., Haidian District, Beijing 100193, China.

[7]CAS Center for Excellence in Topological Quantum Computation, University of Chinese Academy of Sciences, Beijing 100190, China.

*These authors contributed equally to this work.

†Corresponding author. E-mail: jianwangphysics@pku.edu.cn (J.W.); liliwang@mail.tsinghua.edu.cn (L.W.); xilin@pku.edu.cn (X.L.);

Abstract:

Recent emergence of two-dimensional (2D) crystalline superconductors has provided a promising platform to investigate novel quantum physics and potential applications. To reveal essential quantum phenomena therein, ultralow temperature transport investigation on high quality ultrathin 2D superconducting films is critically required, although it has been quite challenging experimentally. Here we report a systematic transport study on the macro-size ambient-stable ultrathin $PdTe_2$ films grown by molecular beam epitaxy. Interestingly, a new type of Ising superconductivity in 2D centrosymmetric materials is revealed by the detection of

large in-plane critical field more than 6 times Pauli limit. Remarkably, in perpendicular magnetic field, the film undergoes the quantum phase transition from a quantum metal to weakly localized metal with the presence of intermediate quantum Griffiths singularity. Our findings lead to a global phase diagram of two-dimensional superconducting system with strong spin-orbit coupling.

Main Text:

Recent developments of the film-growth and device-fabrication techniques have triggered a flurry of intensive investigations on two-dimensional (2D) crystalline superconducting systems, where new quantum phases and quantum phase transitions are attracting tremendous interest in condensed matter physics (*1*). The superconductor-insulator/metal transition (SIT/SMT), as paradigmatic quantum phase transitions, has been widely studied over the past forty years (*2-5*). However, the observation of quantum Griffiths singularity (QGS) of SMT in low-dimensional crystalline superconducting systems (*6-12*), characterized by a divergent critical exponent $z\nu$, challenges the conventional understanding of the quantum phase transition. QGS reveals the profound influence of the quenched disorder on SMT, manifested as the formation of large superconducting rare regions in the ultralow temperature regime (*13*). The size of these superconducting regions keeps increasing with temperature approaching zero Kelvin, and the slow dynamics leads to a divergent critical exponent $z\nu$ of SMT in 2D system (*13, 14*), in stark contrast to constant $z\nu$ observed in conventional quantum phase transitions (*2, 3*).

Another striking phenomenon that contradicts the conventional wisdom during the SIT/SMT is the intermediate quantum metallic state. Owing to Anderson localization, 2D metallic states are prohibited at zero temperature (*15*). Consistent with this, there are only superconducting and insulating ground states and a direct transition between them in the framework of the dirty-boson model (*16*). However, pioneering works on amorphous thin films, as well as recent experiments on crystalline 2D systems report the emergence of intervening quantum metallic state, characterized by the saturating resistance much lower than the normal state resistance (*10, 17-22*). Until now, the existence and the underlying mechanism of the quantum metallic state are still under intensive and wide debate, partially due to its delicate nature and the possible influence of external noise in experiments (*23*). Especially, such quantum metallic states have not been reported in high quality 2D superconducting films grown by molecular beam epitaxy (MBE). Thus, more convincing evidences on this intriguing phenomenon are highly desired, especially in 2D crystalline systems that host robust superconductivity.

Furthermore, the in-plane critical field of 2D superconductors is normally determined by the spin pair breaking effect, i.e. the Pauli limit. Recently, Ising superconductivity with a large in-plane critical field was reported in several 2D crystalline superconductors with in-plane inversion symmetry breaking (*9, 24-27*). The in-plane inversion asymmetry can give rise to the Zeeman-type spin-orbit coupling (SOC), which polarizes the spin of electrons to the out-of-plane orientation

and protects the superconductivity under large parallel magnetic field. The exploration and investigations on 2D superconductors with strong SOC may shed new light on understanding the aforementioned quantum phenomena.

Here we report systematic ultralow temperature transport study on a macro-size ambient-stable superconductors with strong SOC, i.e. atomically-flat ultrathin crystalline $PdTe_2$ films on $SrTiO_3(001)$ substrate prepared by MBE. The superconductivity in these $PdTe_2$ films survives a large in-plane magnetic field up to more than 6 times of the Pauli limit, indicating an anomalous Zeeman-protected Ising superconductivity. Our electronic structure calculations and theoretical analysis unveil a new mechanism of Ising superconductivity (named type-II Ising superconductivity) in 2D centrosymmetric material. Furthermore, by performing ultralow temperature transport measurement down to 15 mK, the sheet resistance of ultrathin $PdTe_2$ film drops and then saturates with decreasing temperature at finite perpendicular magnetic fields, showing the characteristic of quantum metallic state. At higher fields, the film undergoes a quantum metal to weakly localized metal transition, and the effective critical exponent $z\nu$ obtained by finite size scaling (FSS) grows rapidly and diverges when approaching zero temperature and the characteristic field B_c^*, indicating quantum Griffiths singularity. Our work provides a global phase diagram of quantum metallic phase and quantum Griffiths singularity in the type-II Ising superconductor.

The ultrathin crystalline $PdTe_2$ films were grown on 0.05 wt% Nb-doped $SrTiO_3(001)$ substrates via MBE technique (*28*). Figure 1A shows a schematic of lattice structure of layered $PdTe_2$. It is composed of inversion-symmetric Te-Pd-Te layers that show AA stacking along the (0001) direction (*29*). As confirmed by scanning tunneling microscope (STM) observation (a typical STM image of 4-monolayer (ML) $PdTe_2$ film is shown in Fig. S1), the in-plane structure is uniform hexagonal lattice with constant of 4.0 ± 0.1 Å. The 4-ML and 6-ML $PdTe_2$ films have been observed to be superconducting with respective critical transition temperature T_c (defined as the temperature required to reach 50% of the normal state sheet resistance R_n) of 701.5 mK and 734.7 mK (Fig. S3A). Figures 1B and 1C display the in-plane magnetoresistance of 4-ML and 6-ML $PdTe_2$ films up to 9 T. We define in-plane critical field $B_c^{\parallel}$ as the magnetic field required to reach 50% of R_n (dashed lines in Figs. 1B and 1C) and estimated the Pauli limit by B_P (in tesla) $= 1.84T_c$ (in kelvin) (*30, 31*), which is 1.29 T for 4-ML and 1.36 T for 6-ML $PdTe_2$ films. To quantitatively study the superconducting properties of $PdTe_2$ films under parallel magnetic field, we plot $B_c^{\parallel}$ normalized by B_P as a function of T/T_c for 4-ML and 6-ML $PdTe_2$ films in Fig. 1D. Clearly, for 6-ML (4-ML) film, the measured $B_c^{\parallel}$ exceeds 6 times of B_P at $0.48T_c$ ($0.76T_c$), reminiscent of Ising superconductivity. Notably, the $PdTe_2$ ultrathin films studied here are in-plane centrosymmetric (Fig. 1A). Thus, the superconductivity with large in-plane critical field observed here is distinct from the Ising superconductivity in non-centrosymmetric systems (*24-26*) (named type-I Ising superconductivity). Instead, our result can be understood by the mechanism of type-II Ising superconductivity (*32*) that does not require inversion symmetry breaking: For degenerate p_{xy} orbitals at the Γ point, the SOC introduces a so-called spin-orbital locking $H_{SOC} = \beta_{SO}\tau_z\sigma_z$, where β_{SO} represents the SOC

strength and $\sigma_z, \tau_z = \pm 1$ label spin up/down and $p_x \pm ip_y$ orbitals, respectively. As illustrated in Fig. 1E, the Zeeman-like field $\beta_{\mathrm{SO}}\tau_z$ is time-reversal invariant, showing opposite signs for the two opposing orbitals. Importantly, its direction is out-of-plane as ensured by the C_3 rotational symmetry and its magnitude can be extraordinarily large due to the strong SOC. Electron spins are thus strongly polarized along the out-of-plane direction. Figure 1G displays the band structures of 6-ML $PdTe_2$ without and with SOC, which visualizes the SOC-induced splitting for p_{xy} orbitals. First-principles calculations reveal that spin splitting induced by in-plane magnetic field is considerably suppressed by SOC, and the suppression is prominent near Γ and gets weaker with increasing momentum (Fig. 1F). A mean-field $\widetilde{\beta_{\mathrm{SO}}}$ can be used to consider the overall effects for a given Fermi energy. Based on the spin-orbital locking, Ising paring is formed between $(\mathbf{k}\uparrow)_{\tau_z=1}$ and $(-\mathbf{k}\downarrow)_{\tau_z=-1}$ (Fig. 1E). The resulting superconducting states are protected against in-plane magnetic field by the SOC-induced Zeeman-like field, thus displaying upper critical fields significantly exceeding the Pauli limit.

Based on the Gor'kov Green's function technique (*33*), the new microscopic model for the two band type-II Ising superconductor is developed (*28*):

$$\frac{2\omega}{\lambda_0}F\left(\widetilde{\beta_{SO1}},T,B\right)F\left(\widetilde{\beta_{SO2}},T,B\right)+\left(1+\frac{\lambda_-}{\lambda_0}\right)F\left(\widetilde{\beta_{SO1}},T,B\right)+\left(1-\frac{\lambda_-}{\lambda_0}\right)F\left(\widetilde{\beta_{SO2}},T,B\right)=0 \quad (1)$$

with

$$F\left(\widetilde{\beta_{SOr}},T,B\right)=\ln\frac{T}{T_c}+\frac{\mu_B^2B^2}{\widetilde{\beta_{SOr}}^2+\mu_B^2B^2}\left[Re\psi\left(\frac{1}{2}+\frac{i\sqrt{\widetilde{\beta_{SOr}}^2+\mu_B^2B^2}}{2\pi k_BT}\right)-\psi\left(\frac{1}{2}\right)\right], \qquad (r=1,2)$$

and

$$\omega=\lambda_{11}\lambda_{22}-\lambda_{12}\lambda_{21}, \qquad \lambda_-=\lambda_{11}-\lambda_{22}, \qquad \lambda_0=\sqrt{\lambda_-^2+4\lambda_{12}\lambda_{21}}, \qquad \lambda_{12}=\lambda_{21}$$

where $\psi(x)$ is the digamma function. Parameters λ_{11} and λ_{22} represent intraband coupling in band 1 and 2. λ_{12} and λ_{21} denote interband interaction between the two bands. In theory, λ_{11}, λ_{12}, λ_{21} and λ_{22} are intrinsic parameters independent of the external magnetic field direction. To minimize the amount of fitting parameters, we obtained λ_{11}, λ_{12}, λ_{21} and λ_{22} from the theoretical fitting of the perpendicular upper critical field $B_{\mathrm{c2}}^{\perp}$ of the $PdTe_2$ films, which also exhibits the characteristic of two band superconductivity (Fig. S3 and Table S1). As shown in Fig. 1D, the in-plane critical field $B_{\mathrm{c}}^{\parallel}$ of 4-ML and 6-ML $PdTe_2$ films can be well fitted by Eq. 1, yielding the Zeeman-type SOC $\widetilde{\beta_{\mathrm{SO1}}} = 1.836$ meV (band 1), $\widetilde{\beta_{\mathrm{SO2}}} = 1.886$ meV (band 2) for 4-ML films, and $\widetilde{\beta_{\mathrm{SO1}}} = 0.5077$ meV (band 1), $\widetilde{\beta_{\mathrm{SO2}}} = 1.257$ meV (band 2) for 6-ML films, respectively (See Table S2 for all parameters). It is noteworthy to mention that the spin-orbit scattering mechanism, known as the Klemm-Luther-Beasley (KLB) formula (*34*) fails to explain the enhanced $B_{\mathrm{c}}^{\parallel}$ of 6-ML $PdTe_2$ films in the low temperature regime when $T < 0.7T_{\mathrm{c}}$.

Figure 2A presents the Arrhenius plot of $R_{\mathrm{s}}(T)$ curves in a temperature range from 15 mK to 1 K for 4-ML $PdTe_2$ film at different perpendicular magnetic fields. In the relatively high temperature regime, $\log R_{\mathrm{s}}$ scales linearly with T^{-1}, indicative of

an activated behavior, which is usually attributed to the thermally assisted motion of unpaired vortex, namely the thermal creep (*35*). As shown in Fig. 2B, the activation energy $U(B)$ at various magnetic fields are determined by the slope of the linear portion (the dashed black line) in Fig. 2A and can be well fitted by the formula $U(B) = U_0 \ln(B_0/B)$ (*35*) with $U_0 = 2.64$ K and $B_0 = 0.613$ T for the 4-ML $PdTe_2$ film. When the magnetic field is approaching 0.613 T, the activation energy U drops around zero indicating weak pinning of vortices.

In the ultralow temperature regime, when the field is above 0.491 T, the sheet resistance significantly deviates from the activated behavior at T_{QM} (marked as the arrows in Fig. 2A) and then saturates to a finite value with decreasing temperature down to 15 mK, which is the hallmark of quantum metallic state. Here, well-filtered electrical leads (*28*) (See Fig. S2 for more details) are used in our measurement to investigate the quantum metallic state with linear IV curves (the inset of Fig. 2B), demonstrating that the observed resistance saturation in the ultralow temperature regime is reliable. Thus, the extrinsic origin of the resistance saturation due to high frequency noise, reported in recent experiments on 2D $NbSe_2$ and InO_x superconductors (*23*), can be safely excluded.

Moreover, we measured the magnetoresistance of the same sample at 20 mK, which is consistent with the theoretical model of quantum tunneling of vortices (quantum creep) below 0.625 T (Fig. 2C). In the limit of strong dissipation, the sheet resistance of this model can be expressed as follow (*20, 36*):

$$R_s \sim \frac{\hbar}{4e^2}\frac{\kappa}{1-\kappa} \tag{2}$$

$$\kappa \sim \exp\left[\mathrm{C}\frac{\hbar}{e^2}\frac{1}{R_\mathrm{n}}\left(\frac{B - B_{c2}^{\perp}}{B}\right)\right]$$

where C is a dimensionless constant of order unity, R_n is the sheet resistance of the normal state (874.5 Ω for 4-ML $PdTe_2$ film) and $B_{c2}^{\perp}$ is the perpendicular upper critical field. As shown in Fig. 2C, the magnetoresistance at low temperatures (below 100 mK) and relatively low magnetic fields is well fitted by Eq. 2, indicating that the quantum creep plays a key role in this regime (See Table S3 for the fitting parameters). While at larger magnetic fields above 0.63 T, the sheet resistance at 20 mK exhibits a linear magnetic field dependence, showing the characteristic of pinning-free vortex motion (Fig. 2D). It is noteworthy to mention that the magnetic field for free vortex motion at 20 mK obtained from Fig. 2D is close to $B_0 = 0.613$ T of thermally activated behavior in Fig. 2B.

The quantum metallic state is gradually suppressed with increasing magnetic field and the system undergoes a quantum phase transition from quantum metal to weakly localized metal. As shown in Fig. 3A, the sheet resistance increases with decreasing temperature when the magnetic field exceeds 0.98 T, indicating localized metal behavior. To further investigate the quantum phase transition, we measured the magnetoresistance from 20 mK to 600 mK in details. Different from normal superconductor-metal transition, the isotherms of 4-ML $PdTe_2$ film cross each other at a relatively large and well-defined transition region rather than a single critical point

(Fig. 3B). The crossing points of $R_s(B)$ curves at neighboring temperatures are shown as black dots in Fig. 3C, which slightly deviates from the theoretical fitting (the red solid line) using Werthamer-Helfand-Hohenberg theory (*37*) in the ultralow temperature regime. Furthermore, based on the FSS analysis (*2, 3, 28*), the magnetic field dependence of the effective "critical" exponent zv is summarized in Fig. 3D. When approaching the characteristic magnetic field B_c^* and zero temperature, zv grows rapidly and then diverges. The field dependence of zv can be well fitted by the activated scaling law $zv \propto |B_c^* - B|^{-v\psi}$ with the correlation length exponent $v \approx 1.2$ and the tunneling critical exponent $\psi \approx 0.5$ for two dimensional systems (*38, 39*), providing convincing evidence of QGS with the infinite-randomness quantum critical point.

Based on the aforementioned experimental data, we summarize the phase diagram of 4-ML $PdTe_2$ film in Fig. 4. The boundary of 2D superconductivity (the violet solid curve) is defined as the critical magnetic field required to reach the zero resistance within the measurement resolution. The thermal creep and the thermal fluctuation are separated by the red dashed curve, which represents the critical field of 50% of the normal state resistance R_n. The onset critical temperature T_c (the light brown curve) and the crossing points from the $R_s(B)$ curves (the dark brown curve, corresponding to the black spheres in Fig. 3C) show the boundary from the thermal fluctuation and the quantum Griffiths state to the weakly localized metal, respectively. Most importantly, in the ultralow temperature regime, the phase boundary of quantum metal is marked as the light blue curve, indicating the characteristic temperature T_{QM} (the arrows in Fig. 2A) when the sheet resistance deviates from the thermally activated behavior (the dashed black line in Fig. 2A) and begins to saturate. In the moderate magnetic field regime, the thermally assisted vortex creeps is replaced by the quantum tunneling of vortices with decreasing temperature, corresponding to quantum metal region. At higher magnetic fields, quantum fluctuation and the quenched disorder play a dominant role in the quantum phase transitions in the ultralow temperature leading to quantum Griffiths state, where thermal fluctuation is suppressed. Remarkably, the system undergoes a superconductor to quantum metal quantum phase transition, followed by a quantum metal to weakly localized metal transition via the intervening quantum Griffiths state. Our findings provide a global phase diagram of quantum metallic state and quantum Griffiths singularity in the ultrathin $PdTe_2$ film with type-II Ising pairing. This macroscale high-quality transition metal dichalcogenide $PdTe_2$ films down to a few monolayers show ambient-stable superconductivity with various interesting quantum phases, which not only offer an ideal platform for the investigations on unconventional quantum phase transitions but also exhibit great potentials in electronic and spintronic applications.

References and Notes:

1. Y. Saito, T. Nojima, Y. Iwasa, *Nat. Rev. Mater.* **2**, 16094 (2017).
2. S. L. Sondhi, S. M. Girvin, J. P. Carini, D. Shahar, *Rev. Mod. Phys.* **69**, 315-333 (1997).
3. S. Sachdev, *Quantum Phase Transitions*. (Cambridge Univ. Press, Cambridge, 1999).

4. A. M. Goldman, *Int. J. Mod. Phys. B* **24**, 4081-4101 (2010).
5. A. Del Maestro, B. Rosenow, S. Sachdev, *Ann. Phys. (N.Y.)* **324**, 523-583 (2009).
6. Y. Xing *et al.*, *Science* **350**, 542-545 (2015).
7. N. Markovic, *Science* **350**, 509-509 (2015).
8. S. Shen *et al.*, *Phys. Rev. B* **94**, 144517 (2016).
9. Y. Xing *et al.*, *Nano Lett.* **17**, 6802-6807 (2017).
10. Y. Saito, T. Nojima, Y. Iwasa, *Nat. Commun.* **9**, 778 (2018).
11. E. Zhang *et al.*, *Nat. Commun.* **9**, 4656 (2018).
12. Y. Liu *et al.*, arXiv:1809.09353 [cond-mat.supr-con] (25 September 2018).
13. T. Vojta, C. Kotabage, J. A. Hoyos, *Phys. Rev. B* **79**, 024401 (2009).
14. D. S. Fisher, *Phys. Rev. B* **51**, 6411-6461 (1995).
15. E. Abrahams, P. W. Anderson, D. C. Licciardello, T. V. Ramakrishnan, *Phys. Rev. Lett.* **42**, 673-676 (1979).
16. M. P. A. Fisher, *Phys. Rev. Lett.* **65**, 923-926 (1990).
17. D. Ephron, A. Yazdani, A. Kapitulnik, M. R. Beasley, *Phys. Rev. Lett.* **76**, 1529-1532 (1996).
18. C. Christiansen, L. M. Hernandez, A. M. Goldman, *Phys. Rev. Lett.* **88**, 037004 (2002).
19. Y. G. Qin, C. L. Vicente, J. Yoon, *Phys. Rev. B* **73**, 100505 (2006).
20. Y. Saito, Y. Kasahara, J. T. Ye, Y. Iwasa, T. Nojima, *Science* **350**, 409-413 (2015).
21. N. P. Breznay, A. Kapitulnik, *Sci. Adv.* **3**, e1700612 (2017).
22. A. Kapitulnik, S. A. Kivelson, B. Spivak, *Rev. Mod. Phys.* **91**, 011002 (2019).
23. I. Tamir *et al.*, *Sci. Adv.* **5**, eaau3826 (2019).
24. J. M. Lu *et al.*, *Science* **350**, 1353-1357 (2015).
25. Y. Saito *et al.*, *Nat. Phys.* **12**, 144-149 (2016).
26. X. Xi *et al.*, *Nat. Phys.* **12**, 139 (2016).
27. Y. Liu *et al.*, *Phys. Rev. X* **8**, 021002 (2018).
28. See Supplementary Materials for more details.
29. C. Liu *et al.*, *Phys. Rev. Mater.* **2**, 094001 (2018).
30. B. S. Chandrasekhar, *Appl. Phys. Lett.* **1**, 7-8 (1962).
31. A. M. Clogston, *Phys. Rev. Lett.* **9**, 266 (1962).
32. C. Wang *et al.*, arXiv:1903.06660 [cond-mat.supr-con] (15 March 2019).
33. A. A. Abrikosov, L. P. Gorkov, I. E. Dzialochinski, *Methods of Quantum Field Theory in Statistical Physics*. (Prentice-Hall, Englewood Cliffs, NJ, 1963).
34. R. A. Klemm, A. Luther, M. R. Beasley, *Phys. Rev. B* **12**, 877-891 (1975).
35. M. V. Feigelman, V. B. Geshkenbein, A. I. Larkin, *Physica C* **167**, 177-187 (1990).
36. E. Shimshoni, A. Auerbach, A. Kapitulnik, *Phys. Rev. Lett.* **80**, 3352-3355 (1998).
37. N. R. Werthame, E. Helfand, P. C. Hohenber, *Phys. Rev.* **147**, 295 (1966).
38. T. Vojta, A. Farquhar, J. Mast, *Phys. Rev. E* **79**, 011111 (2009).
39. I. A. Kovacs, F. Igloi, *Phys. Rev. B* **82**, 054437 (2010).

Acknowledgements:

We thank X. C. Xie, Wenhui Duan for helpful discussions and Pengjie Wang, Yifang Xu, Qingzheng Qiu for the help in ultralow temperature transport measurement. This work was financially supported by the National Key Research and

Development Program of China (Grant No. 2018YFA0305600, No. 2017YFA0303300, No. 2015CB921000, No. 2015CB921100 and No. 2018YFA0307100), the National Natural Science Foundation of China (Grant No. 11888101, No.11774008, No. 11774193, No. 11790311, No. 51788104, No. 11874035 and No. 11674188), the Strategic Priority Research Program of Chinese Academy of Sciences (Grant No. XDB28000000), Beijing Natural Science Foundation (Z180010) and the Beijing Advanced Innovation Center for Future Chip (ICFC).

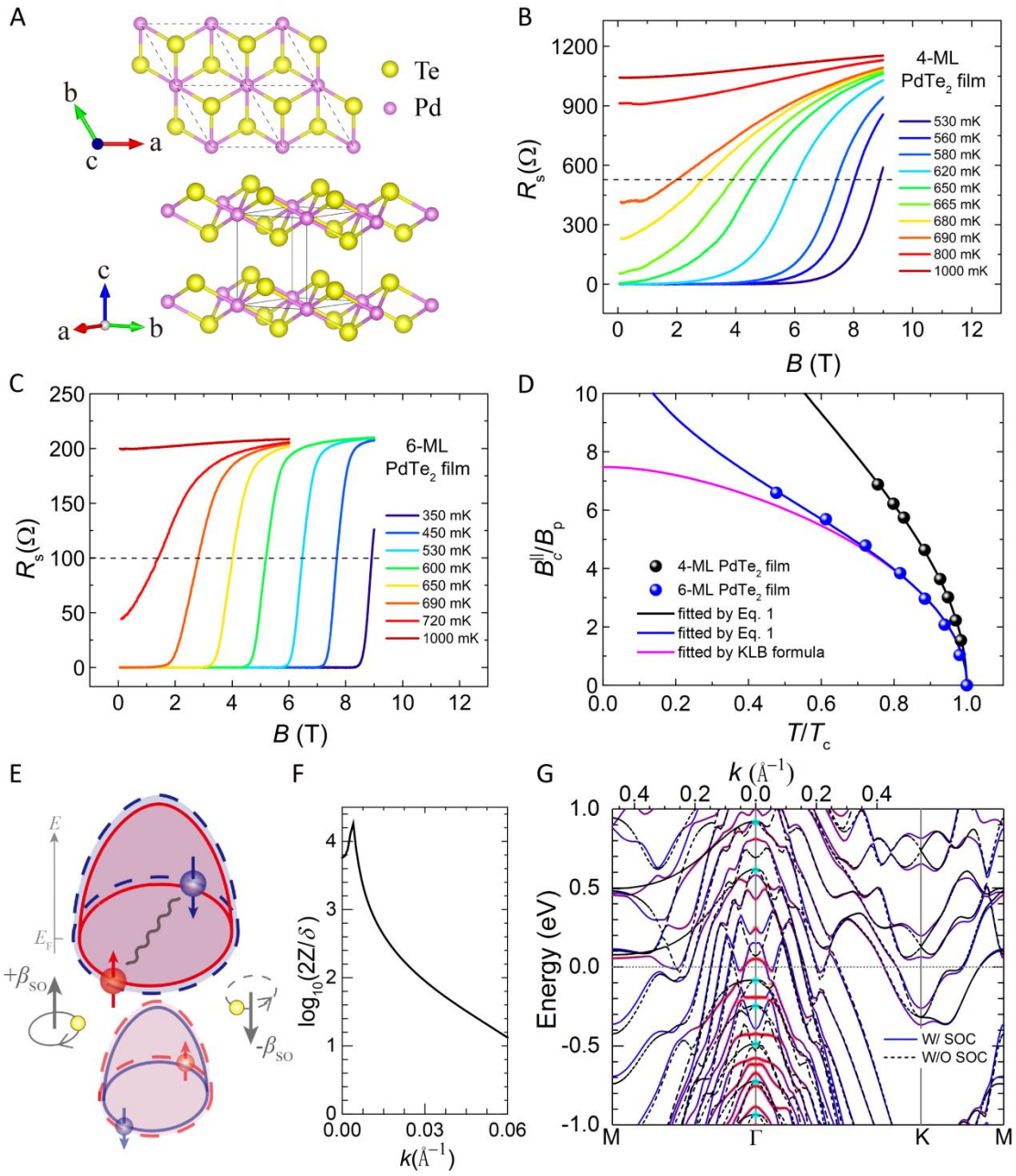

Fig. 1. Type-II Ising superconductivity in 4-ML and 6-ML $PdTe_2$ film. (**A**) The schematic of lattice structure of $PdTe_2$ with in-plane inversion symmetry. (**B**) The parallel magnetic field dependence of the sheet resistance in 4-ML $PdTe_2$ film at different temperatures ranging from 530 mK to 1000 mK. (**C**) The $R_s(B)$ curves of 6-ML $PbTe_2$ film from 350 mK to 1000 mK. (**D**) The in-plane critical field $B_c^{\parallel}$ of 4-ML (the black spheres) and 6-ML (the blue spheres) $PbTe_2$ film. Here, $B_c^{\parallel}$ is defined as the magnetic field required to reach the 50% of the normal state sheet resistance R_n (the dashed lines in Fig. 1(B) and 1(C)). The solid blue and black lines represent the fitting curves using the theoretical formula for type-II Ising superconductor (Eq. 1). The solid magenta line is the fitting curve using KLB formula, which underestimates the $B_c^{\parallel}$ when $T < 0.7T_c$. (**E**) Schematic diagram of type-II Ising superconductivity mechanism. For multiple degenerate orbitals near a high-symmetry point, the SOC results in a spin-orbital locking and generates opposite Zeeman-like fields ($\pm\beta_{SO}$) for the two opposing orbitals (dashed and solid lines), which strongly

polarizes spins (red and blue) along the out-of-plane direction. Type-II Ising superconducting paring formed between opposite spins, momenta and orbitals is thus protected against in-plane magnetic fields, displaying unusually large upper critical fields. (**F**) The calculated ratio between Zeeman splitting without SOC ($2Z$) and with SOC (δ) as a function of momentum (k) referenced to Γ for a near-Fermi-level band of 6-ML $PdTe_2$ contributed by p_{xy} orbitals under an in-plane magnetic field of two Tesla. (**G**) Band structures of 6-ML $PdTe_2$ without (W/O) and with SOC (W/). Bands contributed by p_{xy} orbitals are four-fold degenerate at Γ without SOC (denoted by cyan dots) and become split into two sets of spin-degenerate bands with SOC (colored red).

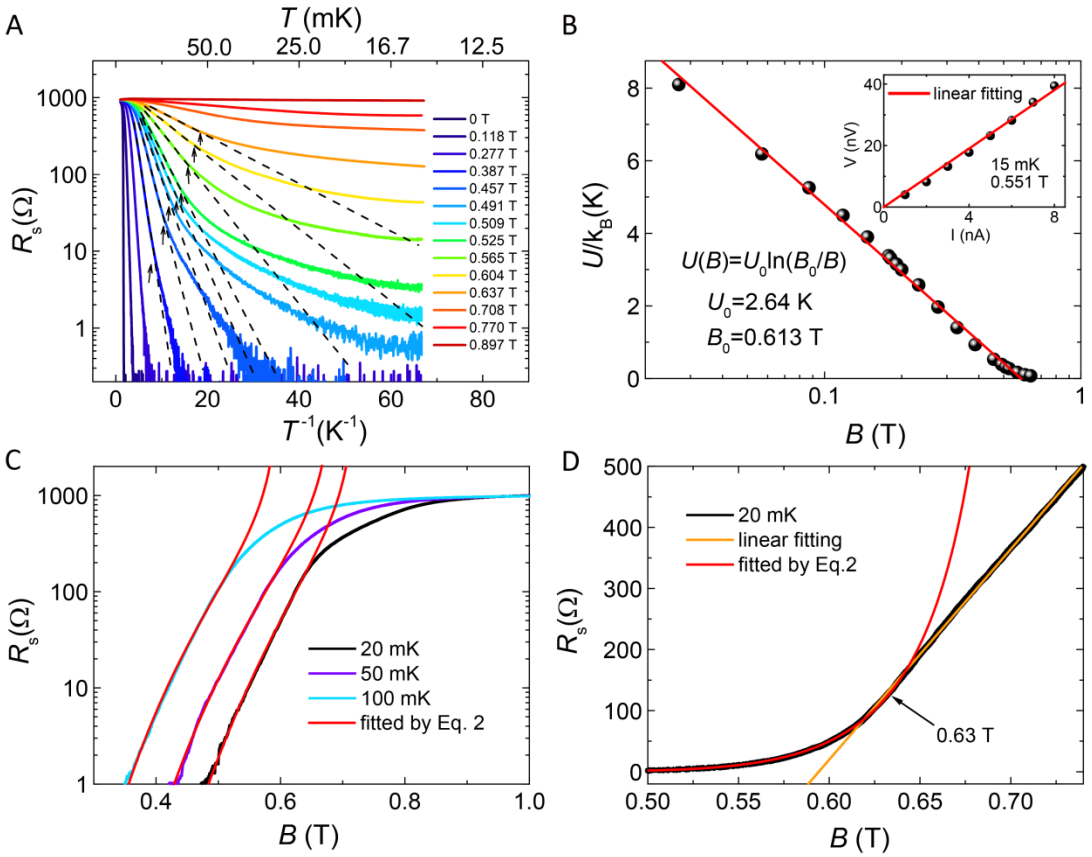

Fig. 2. Evidence for thermally assisted vortex motion and quantum metallic state in 4-ML $PdTe_2$ film. (**A**) Arrhenius plot of the sheet resistance at different perpendicular magnetic fields from 0 T to 0.897 T. The dashed black lines show the activated behavior in the relatively high temperature regime. (**B**) The magnetic field dependence of activation energy *U*, obtained from the slope of the linear portion in Fig. 1A. The inset: the linear IV curve at 20 mK and 0.551 T. (**C**) The $R_s(B)$ curves of 4-ML $PbTe_2$ film at 20, 50 and 100 mK, which can be well fitted by Eq. 2 in the relatively low magnetic field regime (the solid red line). (**D**) The $R_s(B)$ curve exhibits a linear magnetic field dependence above 0.63 T.

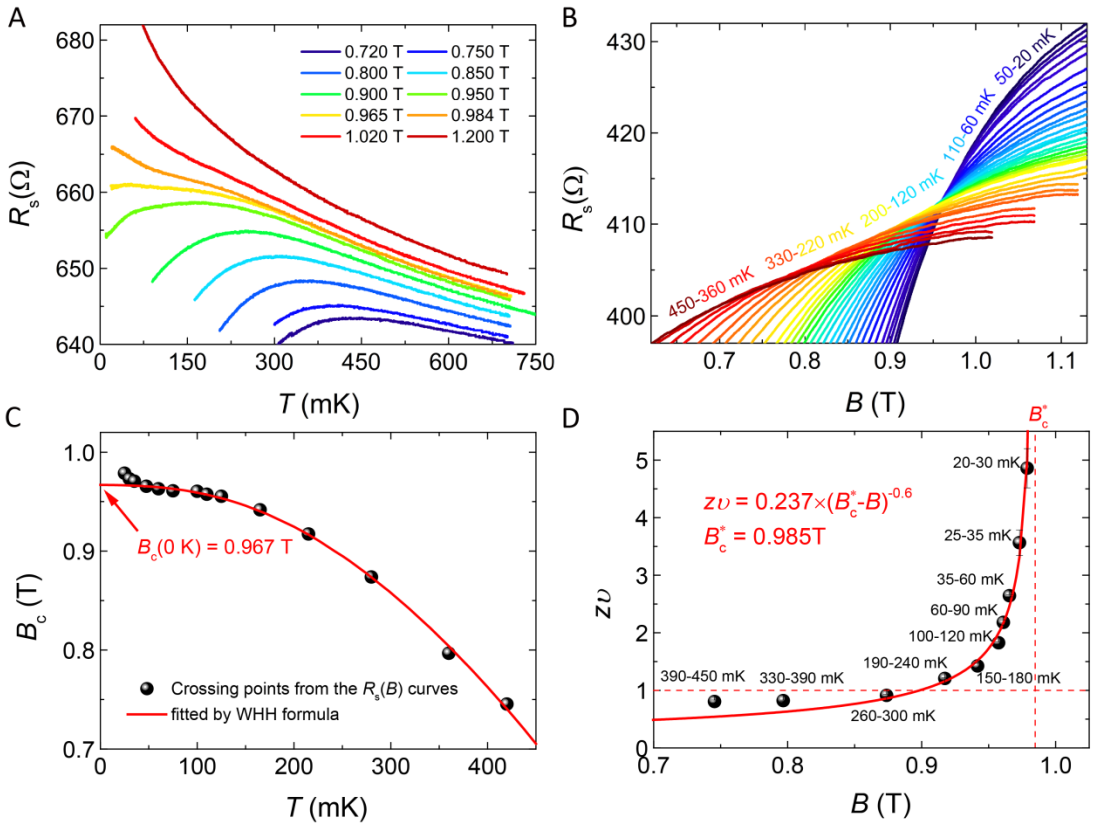

Fig. 3. Quantum Griffiths singularity in 4-ML $PdTe_2$ film. (**A**) The $R_s(T)$ curves at different perpendicular magnetic fields ranging from 0.720 T to 1.200 T. (**B**) The magnetoresistance $R_s(B)$ curves at various temperatures from 20 mK to 450 mK with the same sweep rate and same sweep direction. (**C**) The crossing points of the neighboring $R_s(B)$ curves in Fig. 3B, which slightly deviate from the theoretical fitting using Werthamer-Helfand-Hohenberg theory (the solid red line) in the ultralow temperature regime. (**D**) The effective "critical" exponent $z\nu$ as a function of magnetic field. The solid red line is the fitting curve of the activated scaling law $z\nu \propto |B_c^* - B|^{-0.6}$. The dashed red lines are $z\nu = 1$ and $B = B_c^*$, respectively.

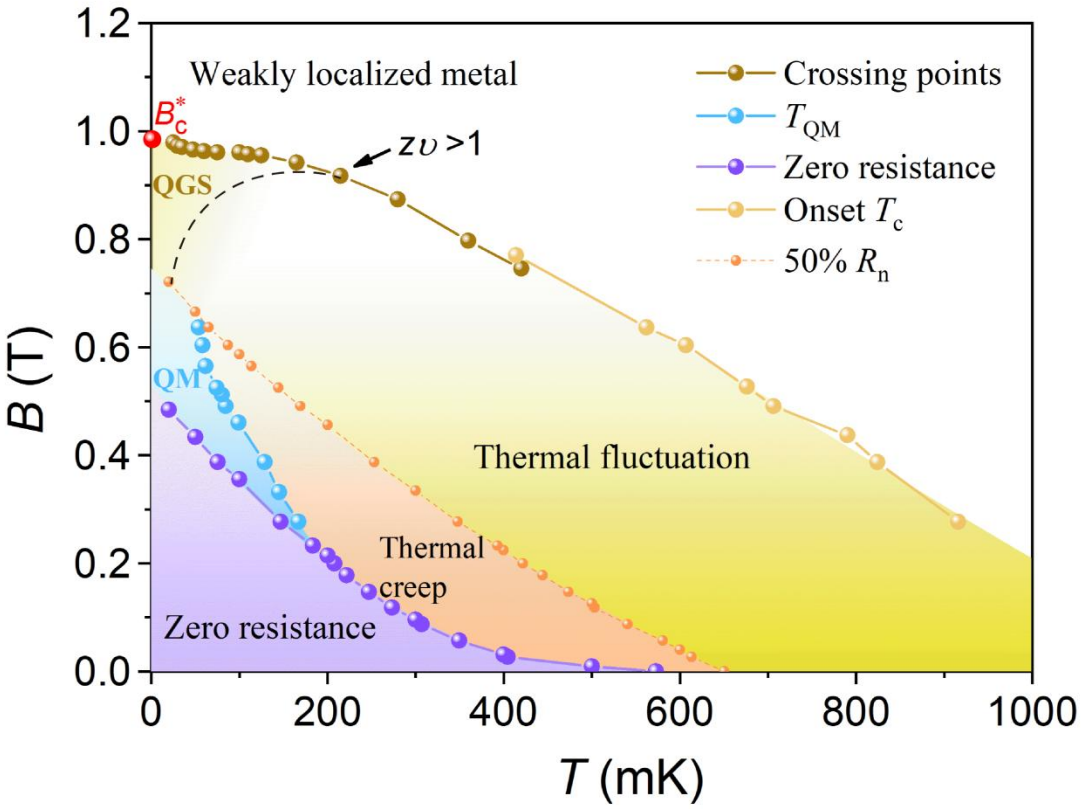

Fig. 4. The complete *B*-*T* phase diagram of 4-ML $PdTe_2$ film. The dark blue and red spheres represent the superconducting critical field of zero resistance and 50% of the normal state sheet resistance R_n, respectively. The dark brown spheres show the crossing points of the neighboring $R_s(B)$ curves in Fig. 3B. The light brown spheres indicate the onset critical temperature T_c. The phase boundary between the quantum metal (marked as QM) and the thermal creep, as well as quantum Griffiths state (marked as QGS) is shown as the light blue spheres, indicating the characteristic temperature T_{QM} when the sheet resistance deviates from the thermally activated behavior (the dashed black line in Fig. 2A) and begins to saturate. The dashed black line is an ill-defined boundary between quantum Griffiths state and thermal fluctuation. At zero temperature, the system undergoes a superconductor to quantum metal quantum phase transition, followed by a quantum metal to weakly localized metal transition via the infinite-randomness quantum critical point B_c^*.

Supplementary Materials for

"Quantum metal state and quantum phase transitions in type-II Ising superconducting films"

Yi Liu,[1,2]* Yong Xu,[2,3]* Jian Sun,[1,2]* Chong Liu,[3]* Yanzhao Liu,[1,2] Chong Wang,[2,3,4] Zetao Zhang,[2,3] Kaiyuan Gu,[1,2] Yue Tang,[1,2] Cui Ding,[3] Haiwen Liu,[5] Hong Yao,[2,3,4] Xi Lin,[1,2,6,7]† Lili Wang,[2,3]† Qikun Xue,[2,3,6] Jian Wang[1,2,3,6,7]†

[1]International Center for Quantum Materials, School of Physics, Peking University, Beijing 100871, China.

[2]Collaborative Innovation Center of Quantum Matter, Beijing 100871, China.

[3]State Key Laboratory of Low-Dimensional Quantum Physics, Department of Physics, Tsinghua University, Beijing 100084, China.

[4]Institute for Advanced Study, Tsinghua University, Beijing 100084, China.

[5]Center for Advanced Quantum Studies, Department of Physics, Beijing Normal University, Beijing 100875, China.

[6]Beijing Academy of Quantum Information Sciences, West Bld. #3, No. 10 Xibeiwang East Rd., Haidian District, Beijing 100193, China.

[7]CAS Center for Excellence in Topological Quantum Computation, University of Chinese Academy of Sciences, Beijing 100190, China.

*These authors contributed equally to this work.

†Corresponding author. E-mail: jianwangphysics@pku.edu.cn (J.W.);

liliwang@mail.tsinghua.edu.cn (L.W.); xilin@pku.edu.cn (X.L.);

This supplement contains:

Materials and Methods:

The 0.05 wt.% Nb-doped $SrTiO_3$(001) was chosen as substrates, and the TiO_2-terminated surface was obtained after being heated to 1100 ℃ in ultrahigh vacuum. The $PdTe_2$ films were grown by co-evaporating Pd (99.995%) and Te (99.9999%) from Knudsen cells with a flux ratio of ~1:2 on the $SrTiO_3$ substrates kept at 120 ℃. The growth rate was approximately 0.07 monolayer per minute. Scanning tunneling microscopy (STM) images were acquired at 4.8 K in a constant current mode, with the bias voltage (V_s) applied to the sample.

The experiments for quantum metal and quantum Griffiths singularity were carried out in a dilution refrigerator (MNK 126-450; Leiden Cryogenics BV) with a base refrigerator temperature below 6 mK. The thermometry was based on a commercial thermometer and checked by a cerium magnesium nitrate susceptibility thermometer. At temperature ≥ 15 mK, the refrigerator temperature and the electron temperature were measured to be equal with use of the temperature dependence of fractional quantum Hall states' longitudinal resistances.

The experiments investigating the type-II Ising superconductivity were performed in another dilution refrigerator (CF-CS81-600; Leiden Cryogenics BV). The parallel magnetic field condition was realized by a piezo-driven sample rotation system (ANR101; Attocube AG) with a readout resolution of ±0.02 ° and stability of ±0.05 °. We checked the thermometry and the electron temperature in the same way with that in MNK 126-450 system, and the electron temperature of the samples is consistent with the refrigerator temperature when above 25 mK.

In all the above-mentioned measurements, standard lock-in techniques were used and the alternating current excitations were selected according to the criteria of linear I-V curves. To filter out external radiation and obtain ultralow electron temperature environment, filters have been used. In MNK 126-450 system, Thermocoax filters (installed from room temperature to sample plate) and home-made low temperature resistor-capacitor (RC) filters (installed at sample plate) are connected in series with each lead of samples. While in CF-CS81-600 system, home-made room temperature RC filters and home-made silver-epoxy filters (installed at the sample plate) are connected in series with each lead of samples. Filters combinations performance was tested via a vector network analyzer (E5071C ENA; Agilent Technologies) in room temperature, the results are shown in Fig. S2A. In general, combination 1 and 2 both provide a good attenuation of more than 45 dB within the frequency measurement range of the analyzer. And the performance of the combination 1 (combination 2) shows an attenuation larger than 90 dB, reaching the analyzer's noise floor for frequency above 200 MHz (1.1 GHz). The cut-off frequency of these two combinations was also measured via a lock-in amplifier (SR830; Stanford Research Systems), and the results are 6 kHz and 16 kHz to combination 1 and 2 respectively (Fig. S2B).

First-principles calculations based on density functional theory (DFT) were performed by the *OpenMX* package (*40, 41*) using norm-conserving pseudo-potentials and the Perdew-Burke-Ernzerhof exchange-correlation functional (*42*). Bloch wavefunctions were expanded by numerical pseudo-atomic orbitals with optimized

radial part *s*2*p*2*d*2*f*1 (*s*3*p*3*d*2*f*1) and a cutoff radius of 7.0 Bohr for Pd (Te) atoms. Spin-orbit coupling (SOC) was included with fully relativistic scheme and *j*-dependent pseudo potentials. Brillouin zone was discretized by a 14×14×1 grid. Convergence criterion of self-consistent calculations was selected to be 10^{-9} Hartree. The geometry structures studied by OpenMX were optimized by Vienna *ab initio* simulation package (VASP) (*43*), using a slab model with a vacuum layer over 15Å and DFT-D3 method (*44*) for van der Waals corrections. The Kohn-Sham Hamiltonian was read from the output of OpenMX and a Zeeman term of in-plane magnetic field was added to calculate the energy splitting of Kramer pairs. At a specific distance away from Γ point, 10 k-points were uniformly selected around Γ to calculate the Zeeman splitting and the averaged splitting was chosen as the Zeeman splitting at a specific distance.

Theoretical fitting for perpendicular upper critical field

The theoretical formula for the perpendicular upper critical field of two band superconductors can be expressed as (*45*)

$$\frac{2\omega}{\lambda_0} f(t,h) f(t,\eta h) + \left(1 + \frac{\lambda_-}{\lambda_0}\right) f(t,\eta h) + \left(1 - \frac{\lambda_-}{\lambda_0}\right) f(t,h) = 0 \qquad \text{(S1)}$$

with $f(t,h) = \ln t + \left[\psi\left(\frac{1}{2} + h\right) - \psi(h)\right]$, $t = \frac{T}{T_c}$, $\eta = \frac{D_2}{D_1}$, $h = \frac{B_{c2}^{\perp} D_1}{2\phi_0 T}$,

and $\omega = \lambda_{11}\lambda_{22} - \lambda_{12}\lambda_{21}$, $\lambda_- = \lambda_{11} - \lambda_{22}$, $\lambda_0 = \sqrt{\lambda_-^2 + 4\lambda_{12}\lambda_{21}}$, $\lambda_{12} = \lambda_{21}$

where $\psi(x)$ is the digamma function. D_1 and D_2 represent intraband diffusivities of bands 1 and 2. ϕ_0 denotes the magnetic flux quantum. Parameters λ_{11} and λ_{22} represent intraband couplings in band 1 and 2. λ_{12} and λ_{21} denote interband couplings between the two bands. As shown in Fig. S3, the perpendicular upper critical field of 4-ML and 6-ML $PdTe_2$ films can be well fitted by Eq. S1 and the fitting parameters are shown in Table S1.

Theoretical formula for two band Ising superconductivity

Based on the perpendicular critical field analysis, we find the system behaves as a two band superconductor. Thus, we assume the superconductivity originates from the different energy band with two different Fermi wave-vector, and we mainly consider the intra-Fermi-surface scattering with two separate mean free time, and neglect the inter-Fermi-surface scattering (*45*). The single band Zeeman-protected Ising superconductivity can be obtained by the Gor'kov Green's function method (*27, 33*). We can phenomenologically generalize the single band Zeeman-protected Ising superconductivity to the two-band case, and join the single band results together in light of the quasi-classical two-band Usadel equations (*45*). Then, the two-band model for the in-plane critical field reads:

$$\frac{2\omega}{\lambda_0}F\left(\widetilde{\beta_{SO1}},T,B\right)F\left(\widetilde{\beta_{SO2}},T,B\right)+\left(1+\frac{\lambda_-}{\lambda_0}\right)F\left(\widetilde{\beta_{SO1}},T,B\right)+\left(1-\frac{\lambda_-}{\lambda_0}\right)F\left(\widetilde{\beta_{SO2}},T,B\right)=0 \quad (S2)$$

with

$$F\left(\widetilde{\beta_{SOr}},T,B\right)=\ln\frac{T}{T_c}+\frac{\mu_B^2B^2}{\widetilde{\beta_{SOr}}^2+\mu_B^2B^2}\left[Re\psi\left(\frac{1}{2}+\frac{i\sqrt{\widetilde{\beta_{SOr}}^2+\mu_B^2B^2}}{2\pi k_BT}\right)-\psi\left(\frac{1}{2}\right)\right], \qquad (r=1,2)$$

and $\omega=\lambda_{11}\lambda_{22}-\lambda_{12}\lambda_{21},\ \lambda_-=\lambda_{11}-\lambda_{22},\ \lambda_0=\sqrt{\lambda_-^2+4\lambda_{12}\lambda_{21}},\ \lambda_{12}=\lambda_{21},$

where $\psi(x)$ is the digamma function. Here, the parameters λ_{ij} for *i*=1,2 and *j*=1,2 have same values as in the perpendicular field case. The parameters $\widetilde{\beta_{\mathrm{SO1}}}$ and $\widetilde{\beta_{\mathrm{SO2}}}$ are effective Zeeman-type SOC strength for band 1 and band 2, which give rise to the large in-plane critical field. We also note that if the two values of Zeeman-type SOC parameters have little difference or the two values have very large difference, the Eq. S2 can go back to the formula of the one-band Zeeman-protected Ising superconductivity.

Finite size scaling analysis of the quantum phase transition

More details of the phase transition region can be obtained by finite size scaling analysis. According to previous theoretical works (*4*, *6*), the critical sheet resistance of samples R_c and magnetic field B_c satisfies the scaling law expressed as: $R_s(B,T) = R_c \cdot F(|B - B_c|T^{-1/z\nu})$, where F is an arbitrary function with $F(0) = 1$, z and ν are the dynamical critical exponent and correlation length exponent, respectively. As mentioned in the main text, the crossing points at adjacent isotherms changes at different temperature. We take the small critical transition region formed by three or four neighboring $R_s(B)$ curves as one "critical point". For instance, $R_c = 614.6\ \Omega$ and $B_c = 0.9787$ T for a transition region from 20 mK to 30 mK. The scaling law can be further rewritten as $R_s(B,t)/R_c = F(|B - B_c|t)$, where parameter $t \equiv (T/T_0)^{-1/z\nu}$ and T_0 is the lowest temperature used in the scaling of the transition region. Ten representative critical points were selected and the results of normalized R_s/R_c as a function of the scaling variable $|B - B_c|t$ are shown in Fig.S5-S7. By adjusting the value of t, curves from various temperatures can collapse into one curve, and $z\nu$ can be extracted by linear fitting of $\ln(T/T_0)$ vs $\ln(t)$. The magnetic field dependence of $z\nu$ is exhibited in Fig. 3B in the main text.

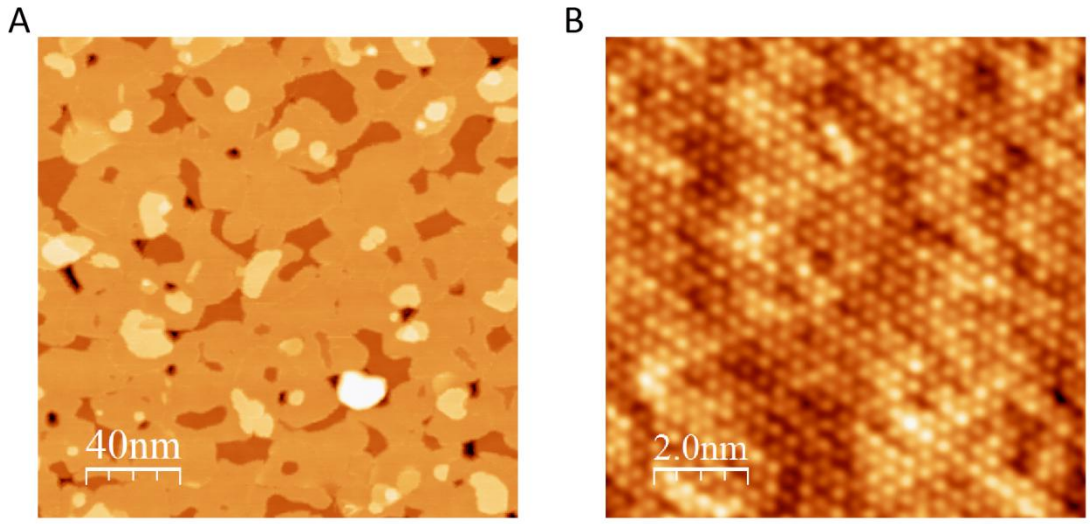

Fig. S1. STM characterization of $PdTe_2$ films. (**A**) A typical STM topographic image of $PdTe_2$ film with a nominal coverage of 4 ML (200 nm × 200 nm, sample bias V_s = 5 V, tunneling current I_t = 100 pA) showing atomically flat crystalline films. (**B**) Atomically resolved STM image (10 nm × 10 nm, V_s = 30 mV, I_t = 1 nA) showing periodic hexagonal lattices with in-plane lattice constant of 4.0 ± 0.1 Å.

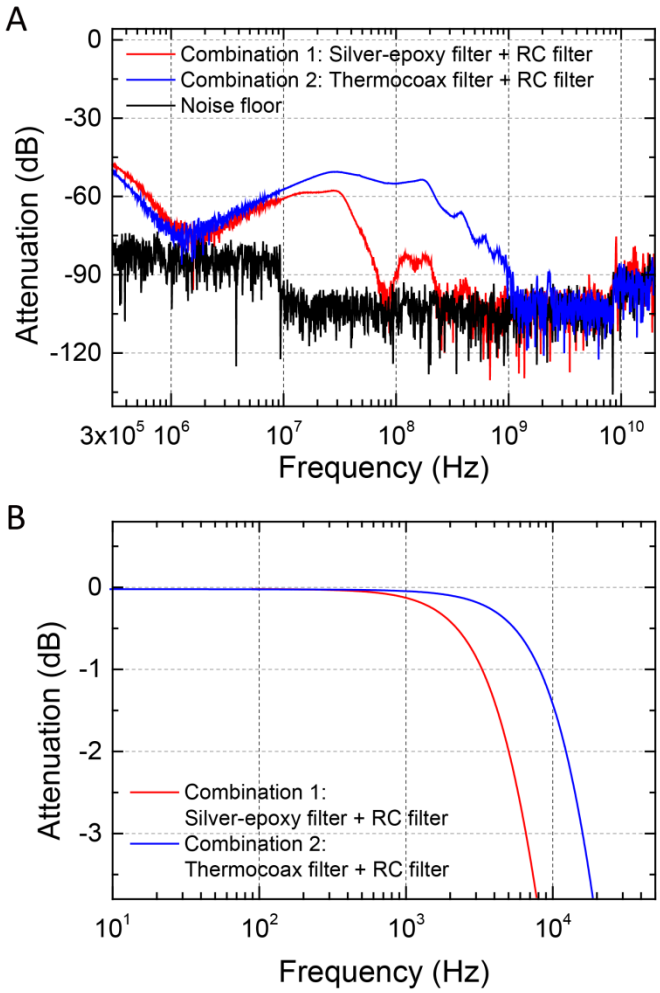

Fig. S2. The performance of filters combinations. (**A**) The graph shows the performance of two filters combinations which are mounted in two dilution refrigerators respectively. Both of them provide a good attenuation, and the combination 1 (2) reaches the analyzer's noise floor (black) for frequency above 200 MHz (1.1 GHz). (**B**) The cut-off frequency of these two combinations is around 6 kHz and 16 kHz to combination 1 and 2 respectively.

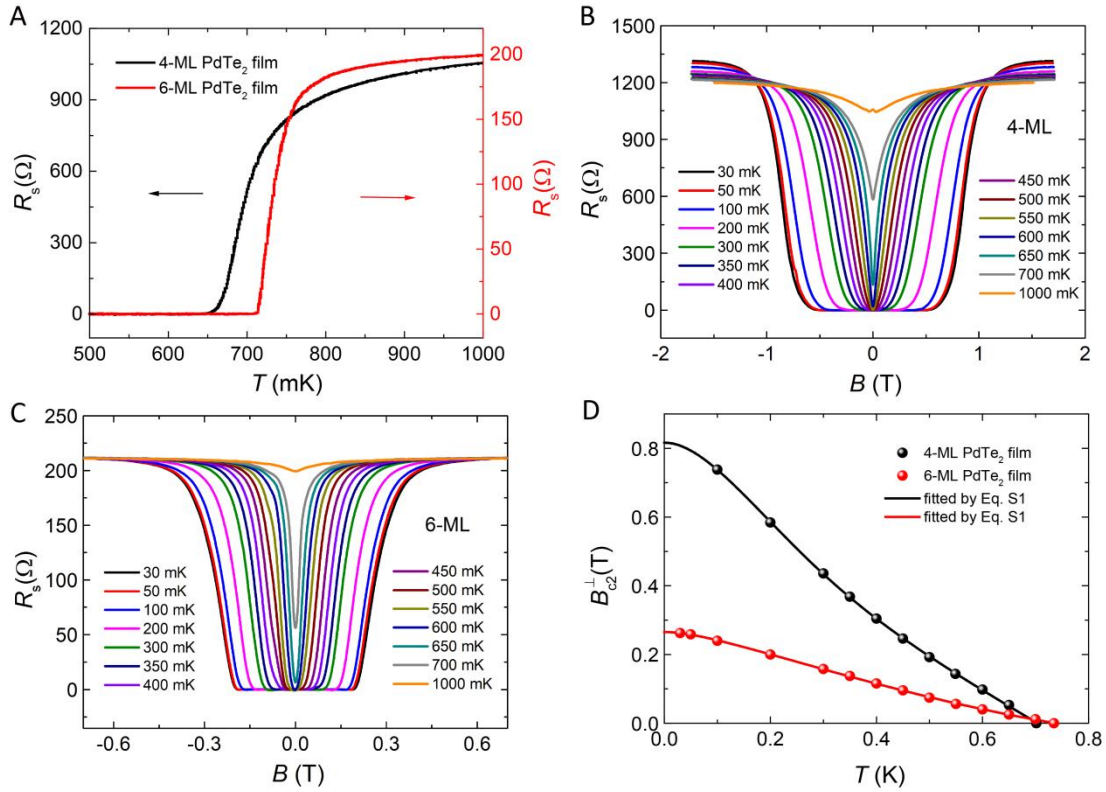

Fig. S3. Superconductivity in ultrathin $PdTe_2$ films at perpendicular magnetic fields. (**A**)The temperature dependence of sheet resistance at 0 T, showing critical transition temperature T_c of 701.5 mK for 4-ML and 734.7 mK for 6-ML $PdTe_2$ films (**B**) (**C**) The perpendicular magnetic field dependence of the sheet resistance in 4-ML (B) and 6-ML (C) $PdTe_2$ films at different temperatures ranging from 30 mK to 1000 mK. (**D**) The upper critical field $B_{c2}^{\perp}$ of 4-ML (the black spheres) and 6-ML (the red spheres) $PbTe_2$ films. Here, $B_{c2}^{\perp}$ is defined as the magnetic field required to reach the 50% of the normal state sheet resistance R_n. The solid black and red lines represent the fitting curves using Eq. S1.

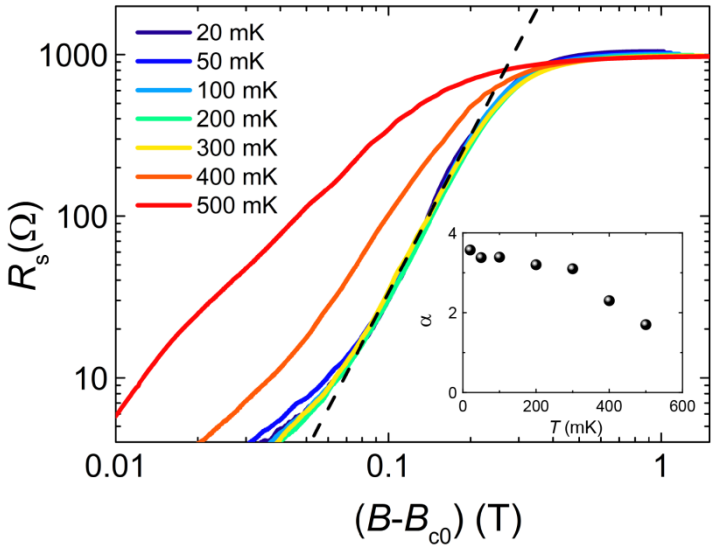

Fig. S4. An alternative explanation of the quantum metallic state is the Bose metal theory, which describes a gapless, nonsuperfluid state in the zero temperature limit (*46-49*). In the framework of this theory, the small residual resistance at finite magnetic fields results from uncondensed Cooper pairs and vortices and the sheet resistance of the metallic state is proportional to $(B - B_{c0})^{2\nu}$, where B_{c0} is the critical field of superconductor to Bose metal transition and ν is the exponent of the superfluid correlation length (*47*). The magnetoresistance $R_s(B - B_{c0})$ curves of 4-ML $PbTe_2$ film is plotted in the double logarithmic scale at various temperatures from 20 mK to 500 mK. The black dashed line indicates the slope of the $R_s(B - B_{c0})$ curves in the low temperature regime. Here, B_{c0} is defined as the critical field of zero resistance within the measurement resolution. The isotherms below 300 mK collapse to a single curve with the slope $\alpha = 2\nu$ slightly larger than 3. The inset shows the slope of the magnetoresistance as a function of temperature, which becomes relatively stable at ultralow temperatures, yielding a critical exponent $\nu \approx 1.72$.

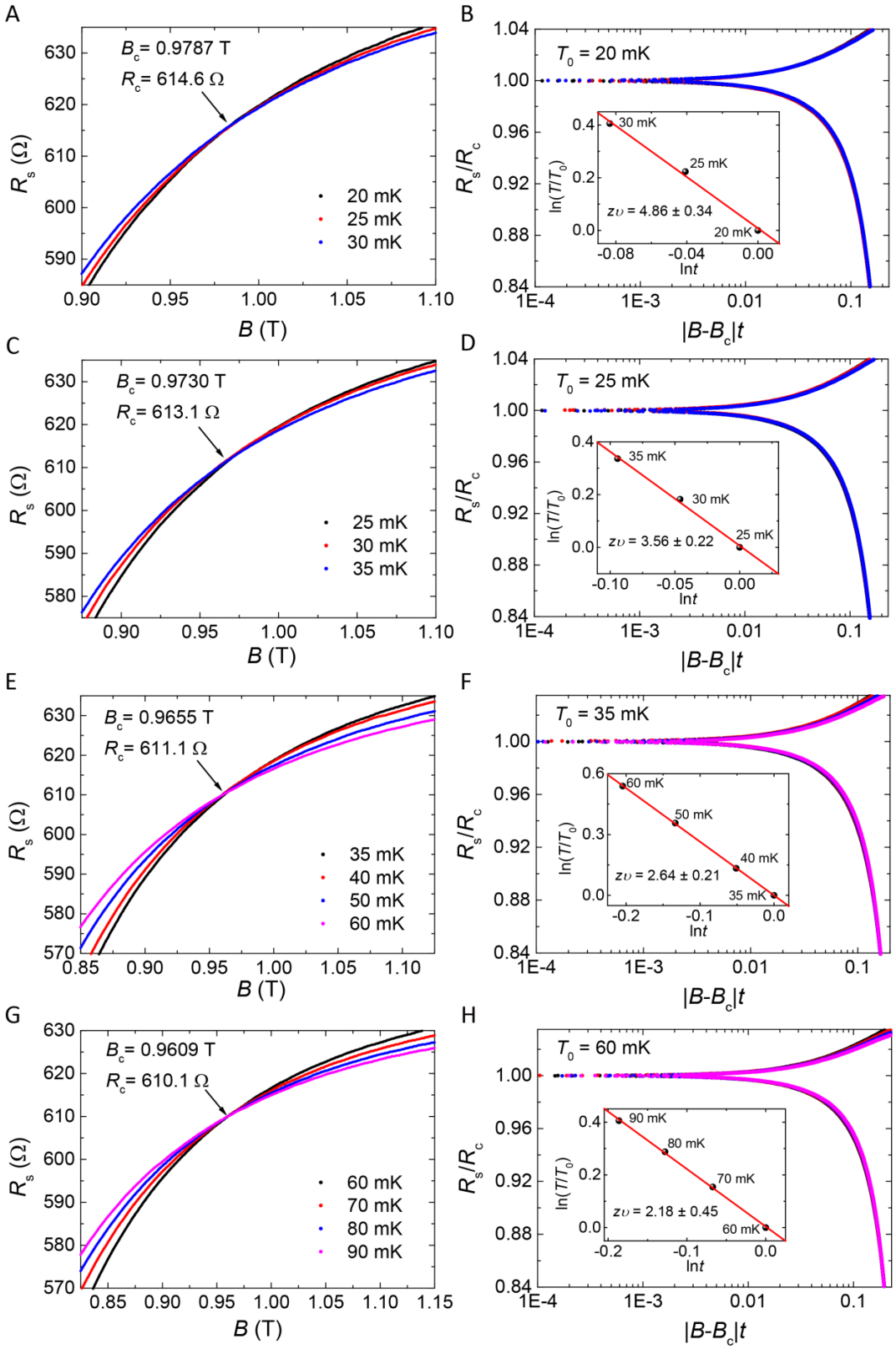

Fig. S5. Finite-size scaling analysis for 4-ML $PdTe_2$ film at temperatures from 20 to 90 mK. (**A**)(**C**)(**E**)(**G**) Sheet resistance as a function of magnetic field at various temperature ranges of (A) 20-30 mK, (C) 25-35 mK, (E) 35-60 mK and (G) 60-90 mK. (**B**)(**D**)(**F**)(**H**) Corresponding normalized sheet resistance as a function of scaling variable $|B - B_c|t$, with $t = T/T_0{}^{-1/z\upsilon}$. Inset: linear fitting between $\ln(T/T_0)$ and $\ln(t)$ gives effective "critical" exponent $z\upsilon$.

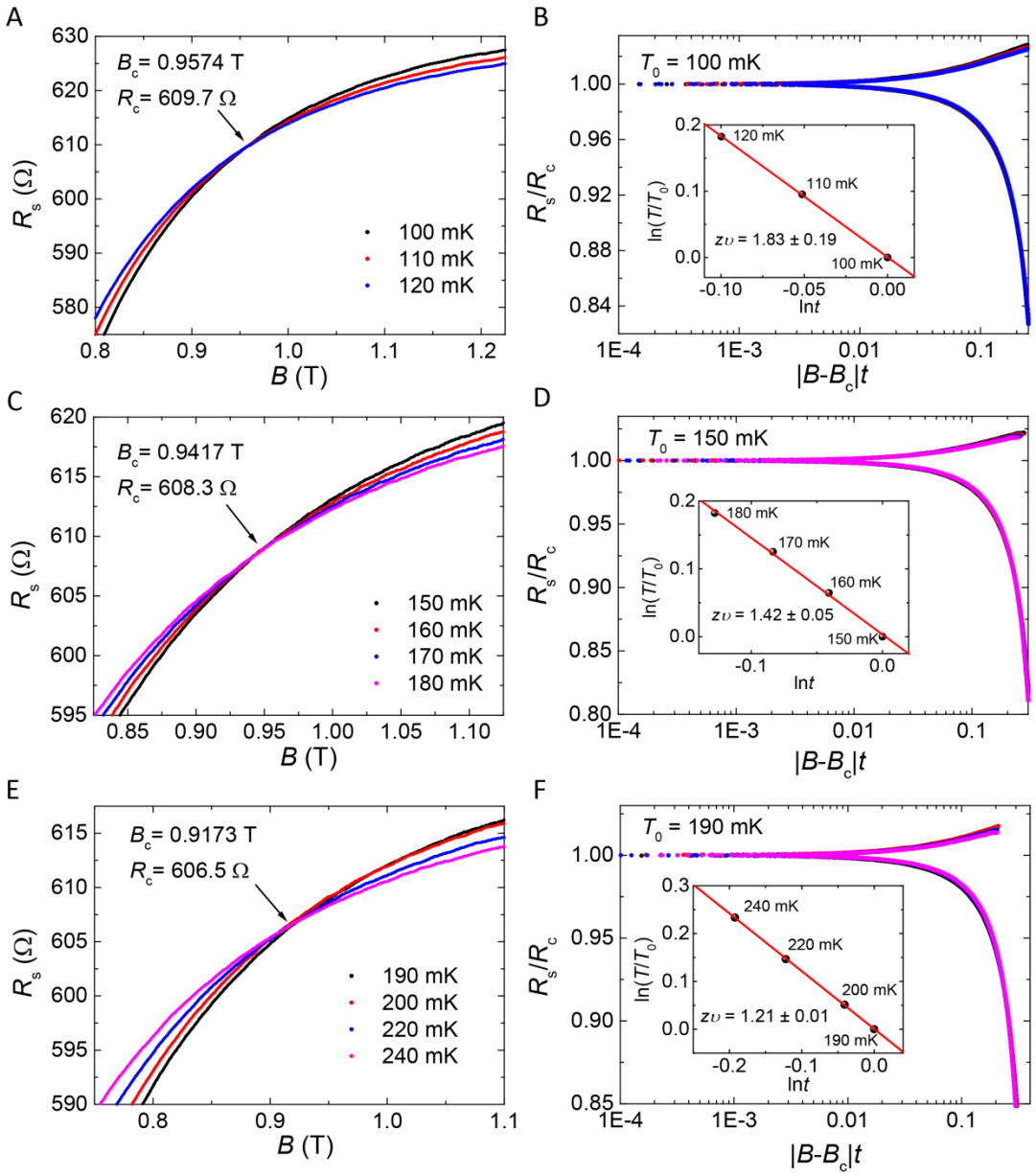

Fig. S6. Finite-size scaling analysis for 4-ML $PdTe_2$ film at temperatures from 100 to 240 mK. (**A**)(**C**)(**E**) Sheet resistance as a function of magnetic field at various temperature ranges of (A) 100-120 mK, (C) 150-180 mK and (E) 190-240 mK. (**B**)(**D**)(**F**) Corresponding normalized sheet resistance as a function of scaling variable $|B - B_c|t$, with $t = T/T_0{}^{-1/z\upsilon}$. Inset: linear fitting between $\ln(T/T_0)$ and $\ln(t)$ gives effective "critical" exponent $z\upsilon$.

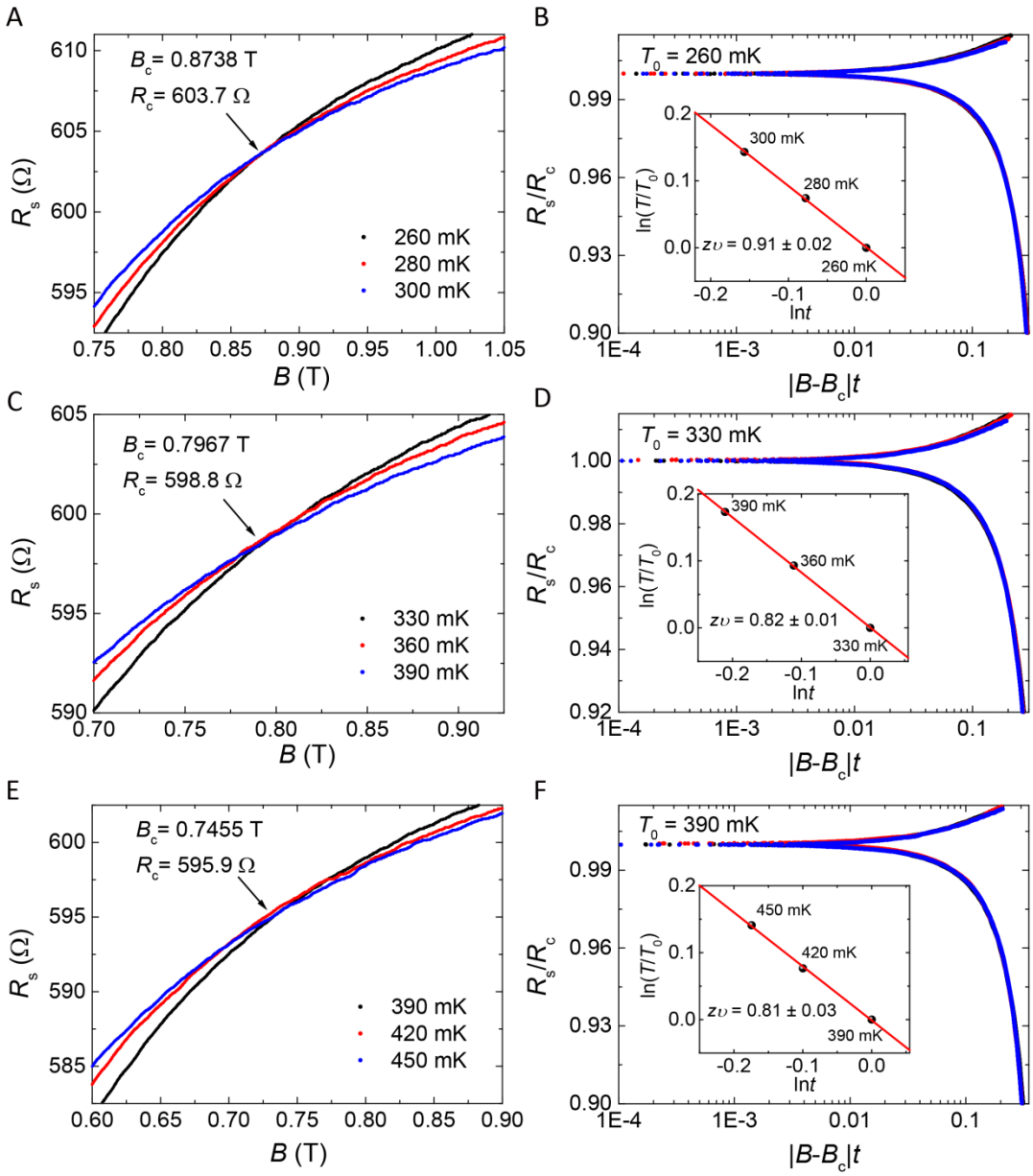

Fig. S7. Finite-size scaling analysis for 4-ML $PdTe_2$ film at temperatures from 260 to 450 mK. (**A**)(**C**)(**E**) Sheet resistance as a function of magnetic field at various temperature ranges of (A) 260-300 mK, (C) 330-390 mK and (E) 390-450 mK. (**B**)(**D**)(**F**) Corresponding normalized sheet resistance as a function of scaling variable $|B - B_c|t$, with $t = T/T_0{}^{-1/z\upsilon}$. Inset: linear fitting between $\ln(T/T_0)$ and $\ln(t)$ gives effective "critical" exponent $z\upsilon$.

Table S1 The fitting parameters of Eq. S1 for the perpendicular upper critical field of 4-ML and 6-ML $PdTe_2$ films.

Thickness	λ_{11}	λ_{12}	λ_{22}	D_1	D_2	T_c/K
4 ML	30.7	19.8	13.9	1.21	0.269	0.704
6 ML	2.74	9.35	29.2	29.0	0.584	0.737

Table S2 The fitting parameters of Eq. 1 for the in-plane critical field of 4-ML and 6-ML $PdTe_2$ films.

Thickness	λ_{11}	λ_{12}	λ_{22}	$\widetilde{\beta_{SO1}}/\,meV$	$\widetilde{\beta_{SO2}}/meV$	T_c/K
4 ML	30.7	19.8	13.9	1.84	1.89	0.701
6 ML	2.74	9.35	29.2	0.508	1.26	0.736

Table S3 The fitting parameters of Eq. 2 for the magnetoresistance of 4-ML $PdTe_2$ films from 20 to 100 mK.

T/mK	C	R_n/Ω	$B_{c2}^{\perp}$/T
20	2.85	874.5	0.721
50	2.34	874.5	0.685
100	1.96	874.5	0.597

References

1. Y. Saito, T. Nojima, Y. Iwasa, *Nat. Rev. Mater.* **2**, 16094 (2017).
2. S. L. Sondhi, S. M. Girvin, J. P. Carini, D. Shahar, *Rev. Mod. Phys.* **69**, 315-333 (1997).
3. S. Sachdev, *Quantum Phase Transitions*. (Cambridge Univ. Press, Cambridge, 1999).
4. A. M. Goldman, *Int. J. Mod. Phys. B* **24**, 4081-4101 (2010).
5. A. Del Maestro, B. Rosenow, S. Sachdev, *Ann. Phys. (N.Y.)* **324**, 523-583 (2009).
6. Y. Xing *et al.*, *Science* **350**, 542-545 (2015).
7. N. Markovic, *Science* **350**, 509-509 (2015).
8. S. Shen *et al.*, *Phys. Rev. B* **94**, 144517 (2016).
9. Y. Xing *et al.*, *Nano Lett.* **17**, 6802-6807 (2017).
10. Y. Saito, T. Nojima, Y. Iwasa, *Nat. Commun.* **9**, 778 (2018).
11. E. Zhang *et al.*, *Nat. Commun.* **9**, 4656 (2018).
12. Y. Liu *et al.*, arXiv:1809.09353 [cond-mat.supr-con] (25 September 2018).
13. T. Vojta, C. Kotabage, J. A. Hoyos, *Phys. Rev. B* **79**, 024401 (2009).
14. D. S. Fisher, *Phys. Rev. B* **51**, 6411-6461 (1995).
15. E. Abrahams, P. W. Anderson, D. C. Licciardello, T. V. Ramakrishnan, *Phys. Rev. Lett.* **42**, 673-676 (1979).
16. M. P. A. Fisher, *Phys. Rev. Lett.* **65**, 923-926 (1990).
17. D. Ephron, A. Yazdani, A. Kapitulnik, M. R. Beasley, *Phys. Rev. Lett.* **76**, 1529-1532 (1996).
18. C. Christiansen, L. M. Hernandez, A. M. Goldman, *Phys. Rev. Lett.* **88**, 037004 (2002).
19. Y. G. Qin, C. L. Vicente, J. Yoon, *Phys. Rev. B* **73**, 100505 (2006).
20. Y. Saito, Y. Kasahara, J. T. Ye, Y. Iwasa, T. Nojima, *Science* **350**, 409-413 (2015).
21. N. P. Breznay, A. Kapitulnik, *Sci. Adv.* **3**, e1700612 (2017).
22. A. Kapitulnik, S. A. Kivelson, B. Spivak, *Rev. Mod. Phys.* **91**, 011002 (2019).
23. I. Tamir *et al.*, *Sci. Adv.* **5**, eaau3826 (2019).
24. J. M. Lu *et al.*, *Science* **350**, 1353-1357 (2015).
25. Y. Saito *et al.*, *Nat. Phys.* **12**, 144-149 (2016).
26. X. Xi *et al.*, *Nat. Phys.* **12**, 139 (2016).
27. Y. Liu *et al.*, *Phys. Rev. X* **8**, 021002 (2018).
28. See Supplementary Materials for more details.
29. C. Liu *et al.*, *Phys. Rev. Mater.* **2**, 094001 (2018).
30. B. S. Chandrasekhar, *Appl. Phys. Lett.* **1**, 7-8 (1962).
31. A. M. Clogston, *Phys. Rev. Lett.* **9**, 266 (1962).
32. C. Wang *et al.*, arXiv:1903.06660 [cond-mat.supr-con] (15 March 2019).
33. A. A. Abrikosov, L. P. Gorkov, I. E. Dzialochinski, *Methods of Quantum Field Theory in Statistical Physics*. (Prentice-Hall, Englewood Cliffs, NJ, 1963).
34. R. A. Klemm, A. Luther, M. R. Beasley, *Phys. Rev. B* **12**, 877-891 (1975).
35. M. V. Feigelman, V. B. Geshkenbein, A. I. Larkin, *Physica C* **167**, 177-187 (1990).
36. E. Shimshoni, A. Auerbach, A. Kapitulnik, *Phys. Rev. Lett.* **80**, 3352-3355 (1998).
37. N. R. Werthame, E. Helfand, P. C. Hohenber, *Phys. Rev.* **147**, 295 (1966).
38. T. Vojta, A. Farquhar, J. Mast, *Phys. Rev. E* **79**, 011111 (2009).
39. I. A. Kovacs, F. Igloi, *Phys. Rev. B* **82**, 054437 (2010).
40. T. Ozaki, *Phys. Rev. B* **67**, 155108 (2003).
41. T. Ozaki, H. Kino, *Phys. Rev. B* **69**, 195113 (2004).

42. J. P. Perdew, K. Burke, M. Ernzerhof, *Phys. Rev. Lett.* **77**, 3865 (1996).
43. G. Kresse, J. Furthmuller, *Phys. Rev. B* **54**, 11169 (1996).
44. S. Grimme, J. Antony, S. Ehrlich, H. Krieg, *J. Chem. Phys.* **132**, 154104 (2010).
45. A. Gurevich, *Phys. Rev. B* **67**, 184515 (2003).
46. D. Das, S. Doniach, *Phys. Rev. B* **60**, 1261-1275 (1999).
47. D. Das, S. Doniach, *Phys. Rev. B* **64**, 134511 (2001).
48. D. Dalidovich, A. Phillips, *Phys. Rev. Lett.* **89**, 027001 (2002).
49. P. Phillips, D. Dalidovich, *Science* **302**, 243-247 (2003).